Contents lists available at ScienceDirect

Transactions of Nonferrous Metals Society of China

36(2026) 830−841

www.tnmsc.cn

Deformation kinking behavior of refractory multi-principal element alloy fabricated by laser additive manufacturing

Yan-song ZHANG [a,b], Hua-ming WANG [a,b], Yan-yan ZHU [a,b,*], Bing-sen LIU [a,b], Zhuo LI [a,b], Bing SU [a,b], Chun-jie SHEN [a,b]

[a] School of Materials Science and Engineering, Beihang University, Beijing 100191, China;

[b] National Engineering Laboratory of Additive Manufacturing for Large Metallic Components, Beijing 100191, China

Abstract: The deformation characteristics and activation mechanisms of kink bands in refractory multi-principal element alloys with local chemical fluctuations (LCFs) were systematically studied. These alloys were fabricated using laser-directed energy deposition technology and characterized by room-temperature compression testing, electron backscatter diffraction (EBSD), transmission electron microscopy (TEM), and high-angle annular dark-field (HAADF) imaging. The results reveal that kinking is a gradual rotational diffusion process, during which the misorientation difference between the kink and the matrix varies. A low Schmid factor is a prerequisite for kink excitation. The slip system closest to the loading axis is passively activated by the applied external force, leading to the accumulation of geometrically necessary dislocations (GNDs) required for lattice rotation. The widespread LCFs within the matrix reduce the migration rate of edge dislocations, promoting GND accumulation and enhancing the propensity for kink band formation. During deformation, the occurrence of kinking enables continuous lattice rotation to accommodate the exceptionally high strain in the vicinity, when the stress concentration in the primary kink cannot be fully released, double kinks are activated to reduce strain energy.

Keywords: refractory multi-principal element alloys; plastic deformation; kink band; Schmid factor; local chemical fluctuation

1 Introduction

Since the concept of multi-principal element alloys (MPEAs) was proposed, it has revolutionized the design strategy of traditional single-principal element alloys (SPEAs), broadening the scope for the development of novel alloys [1−3]. Due to the higher mixing entropy of MPEAs, solid solutions with higher alloying contents are more easily achieved, and the strengthening effect of multi-component solid solutions is more pronounced than that of single-component alloys [4−6]. Refractory MPEAs (RMPEAs) have garnered more attention than other metals due to their high melting temperatures and strengths. However, RMPEAs generally exhibit low ductility, exemplified by WMoNbTa and WMoNbTaV alloys [7]. WANG et al [8] noted that the brittleness of WMoNbTa alloy results from poor grain boundary bonding caused by oxygen segregation, and that boron atom modification significantly enhances plasticity, achieving values exceeding 10%. Thus, ductility in RMPEAs can be enhanced through various strategies, including grain boundary engineering [8], metastability engineering [9], and microstructure reversal [10,11]. Recently, some RMPEAs have demonstrated excellent plasticity due to their distinctive deformation mechanisms. The $Hf_{15}Nb_{40}Ta_{25}Ti_{15}Zr_5$ (at.%) alloy exhibits excellent cold working deformability at room temperature, attributed to the formation of significant kink bands during cold-rolling deformation [12]. Although less

Corresponding author: *Yan-yan ZHU, Tel: +86-13811024443, E-mail: zhuyy@buaa.edu.cn

https://doi.org/10.1016/S1003-6326(25)67000-2

Received 14 June 2024; accepted 28 April 2025

common than twinning, kink behavior remains a necessary complementary deformation mechanism for materials with strong plastic anisotropy, such as Zn crystals [13].

Kinking behavior is nearly universal during RMPEA deformation, particularly in recently developed laser-additively manufactured RMPEAs [14−17]. Existing research indicates that kink behavior is a vital deformation mode in body-centered cubic (BCC) RMPEAs for alleviating stress concentration [18−20]. Some RMPEAs composed of light refractory elements (Ti, Zr, Nb, V, Al, etc.) have demonstrated a well-balanced combination of strength and ductility [21−23]. Previous studies [24] have shown that this series of alloys exhibit substantial kink behavior during deformation, ensuring excellent deformability.

However, a targeted understanding of the specific microstructural characteristics, driving activation factors, and deformation pathways of kink behavior in RMPEAs remains lacking. In this work, we have selected the $Al_{4.4}Nb_{14.7}Ti_{44.1}V_{14.7}Zr_{22.1}$ alloy as a model system, produced via laser-directed energy deposition (LDED) technology, and have conducted a detailed analysis of the orientation characteristics and microstructure of kink bands. Our focus has been on examining the relationship between loading direction and kink behavior activation through specific slip systems, as well as investigating the fundamental cause of frequent kinking in RMPEAs. This work is crucial for advancing our fundamental understanding of RMPEAs' plastic deformation and their potential engineering applications. It provides new insights into the optimal design of ductile RMPEAs that enhance kinking behavior.

2 Experimental

2.1 Powder materials and manufacturing process

The alloy with the nominal composition of $Al_{4.4}Nb_{14.7}Ti_{44.1}V_{14.7}Zr_{22.1}$ (at.%) alloy was fabricated using LDED technology. The fabrication process was carried out in an LDED additive manufacturing system equipped with a 10 kW fiber laser, four-axis CNC machinery, an argon-protected chamber, and a coaxial powder feeding system. The pre-alloyed powders of $Al_{4.4}Nb_{14.7}Ti_{44.1}V_{14.7}Zr_{22.1}$ (at.%) were produced by plasma rotation electrode atomization at Xi'an Sailong AM Technologies Co., Ltd., China. The schematic diagram of alloy deposition, and the morphology and size of the powder, are shown in Fig. 1(a). The deposition process parameters were as follows: output power of 5.5−6 kW, powder delivery rate of 800−1000 g/h, and scanning speed of 1000 mm/min. The entire preparation process was carried out in an argon-protected atmosphere, with an oxygen content below 80×10^{-6}, resulting in the formation of a plate, as shown in Fig. 1(b). The newly deposited alloy plate was immediately tempered at 600 °C for 2 h to relieve residual stresses, followed by homogenization at 1100 °C for 1 h with water quenching.

2.2 Mechanical properties testing and microstructural characterization

Mechanical compression tests were conducted using an electrohydraulic universal tester at a strain rate of $1\times10^{-3}\ s^{-1}$. Cylindrical samples with dimensions of d4 mm × 4 mm were used, with their heights aligned parallel to the deposition direction during additive manufacturing. The compressed samples were split along the cylindrical axis, and the cross-sectional surfaces were polished using SiC emery paper and SiO_2 slurry for subsequent microstructure observation. The entire sample preparation, deformation, and cutting process are shown in Fig. 1(c). Phase identification was performed using X-ray diffraction (XRD, D/MAX−2500). Electron backscatter diffraction (EBSD) analysis was performed using a JEOL JSM 7900 F scanning electron microscope (SEM). Further nano-structural characterization post-deformation was conducted using a transmission electron microscope (TEM, FEI F20). High-angle annular dark-field scanning transmission electron microscopy (HAADF-STEM) analysis was performed using the FEI Themis Z electron microscope, which was operated at 300 kV.

3 Results and discussion

3.1 Primary microstructure before deformation

The primary EBSD morphology and microstructure of the alloy are presented in Fig. 2. The alloy exhibits alternating morphologies of equiaxed and columnar grains along the deposition direction, as shown in Figs. 2(a, b). This phenomenon is attributed to the nucleation and growth mechanism within the single melt pool during the layer-by-layer deposition process [25]. Equiaxed grains form at the

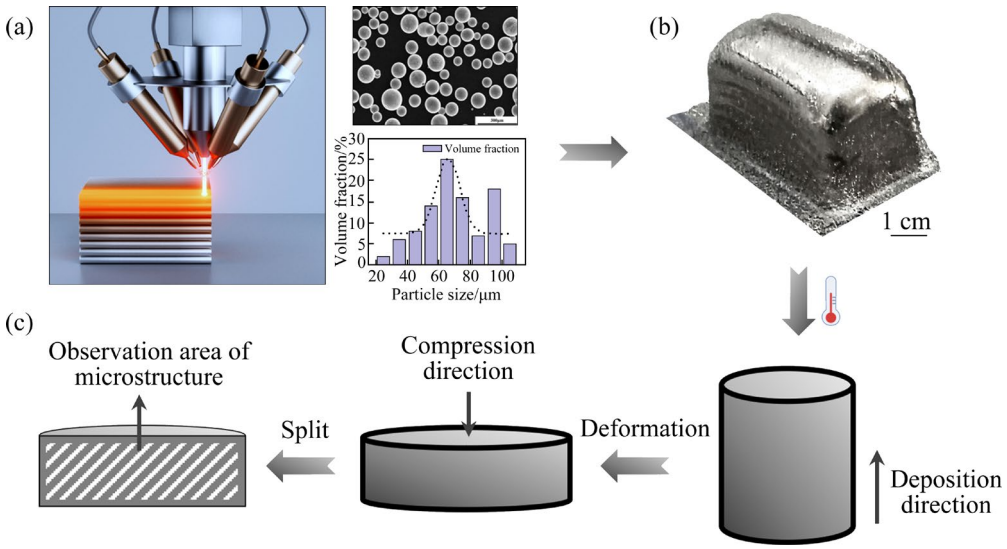

Fig. 1 Experimental method diagram: (a) Laser deposition schematic diagram, morphology and size of powder; (b) Specimen fabricated by LDED of RMPEA; (c) Schematic diagram of sample processing, compression direction, and microstructure testing area

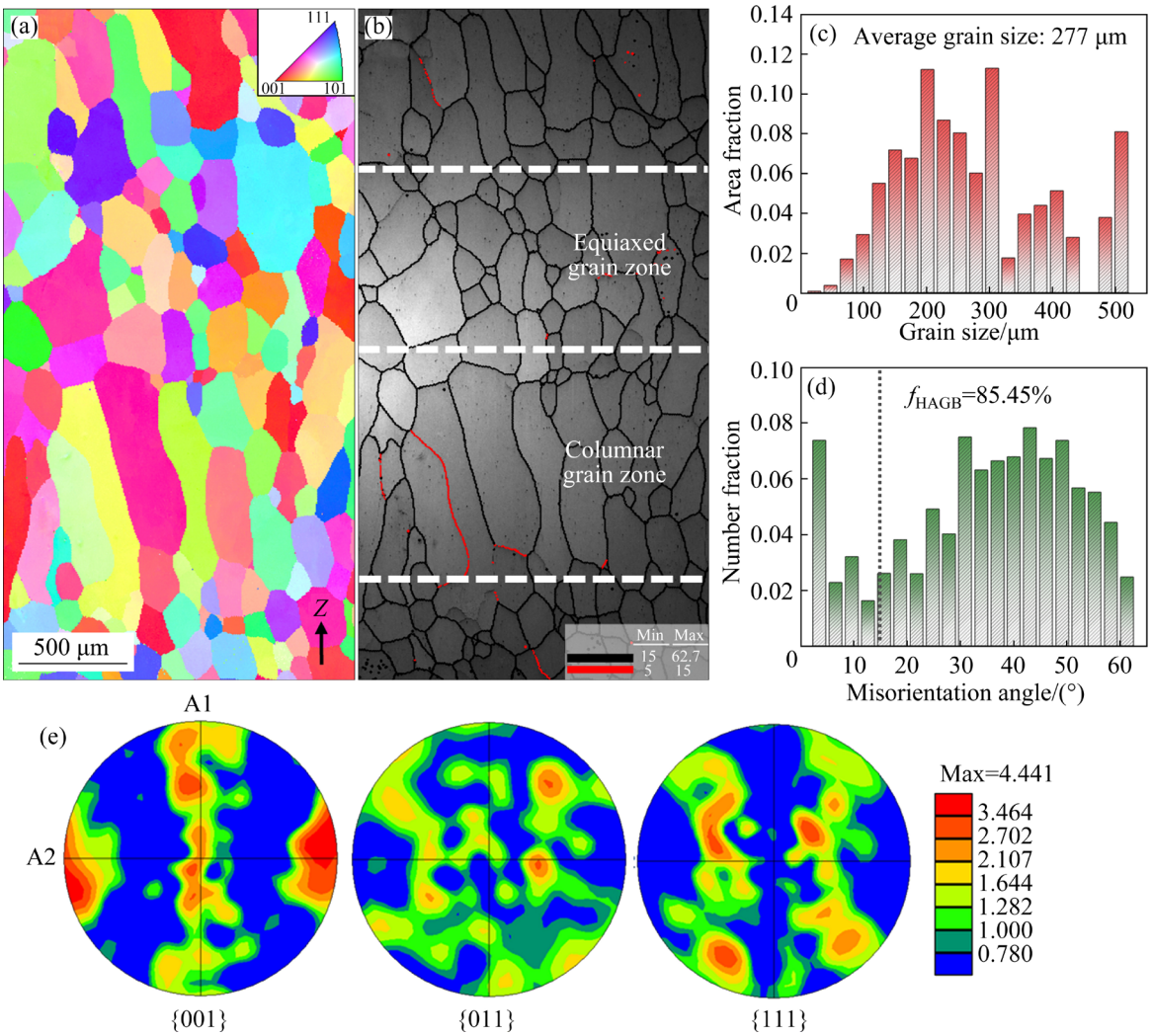

Fig. 2 EBSD results of LDED-RMPEA: (a) Inverse pole figure (IPF) along *Z*-direction; (b) Image quality (IQ) maps; (c) Grain size distribution; (d) Misorientation angle distribution; (e) Pole figures

top of the melt pool due to the heterogeneous nucleation of partially melted powder, while columnar grains grow epitaxially from the bottom. When the remelting depth of the next layer does not penetrate the equiaxed grain layer, it results in the formation of bimodal grain morphology, averaging 277 μm in grain size, as shown in Fig. 2(c). High-angle grain boundaries (HAGBs) with orientation deviations exceeding 15° constitute approximately 85.45% of the alloy, as shown in Fig. 2(d). A high-volume fraction of HAGBs can accommodate more dislocations during deformation, as demonstrated in Ref. [26]. Despite the tendency for epitaxial growth in grain morphology, significant grain competition does not occur due to the limited epitaxial growth distance, and no noticeable texture is observed in the alloy, as shown in Fig. 2(e).

The phase characterization of the sample reveals a single-phase solid solution with a BCC structure, as shown in Fig. S1 in Supplementary Material (SM), with no additional precipitates observed. Figure 3(a) shows the representative TEM bright-field image of the sample, featuring smooth grain boundaries, no precipitation, and only stress fringes within the grains. The corresponding diffraction spots, without superlattice spots, are consistent with the XRD results. However, additional nanoclusters were observed in the BCC matrix in the dark-field image, as shown in Fig. 3(d), which is captured under the diffraction condition indicated by the yellow dashed circle in Fig. 3(c). A noticeable mismatch distortion between the nanocluster and the matrix is evident in the high-resolution (HR) TEM image (see Fig. 3(e), yellow dotted circle). The fast Fourier transform (FFT) pattern in Fig. 3(f) indicates that the clusters do not exhibit ordered characteristics. A high lattice strain distribution is observed in this region, as shown in Fig. 3(g). Figure 3(h) presents the HAADF-STEM micrograph of this alloy under the [001] zone axis. The variation in image contrast arises from *Z*-contrast, where lighter-atom-rich regions appear darker and heavier-atom-rich regions appear brighter.

This observation indicates the presence of local chemical fluctuations (LCFs) within the alloy, arising from atomic-scale chemical deviations that do not result in the formation of nanoscale precipitates [27−29]. Based on the mixing enthalpy data for each element, we propose that the LCFs in this alloy are primarily driven by the strong affinity between Al and Zr atomic pairs. This inference is reasonable, as Al- and Zr-enriched B2 domains and Al−Zr intermetallic compounds are commonly identified in multi-component alloys of similar

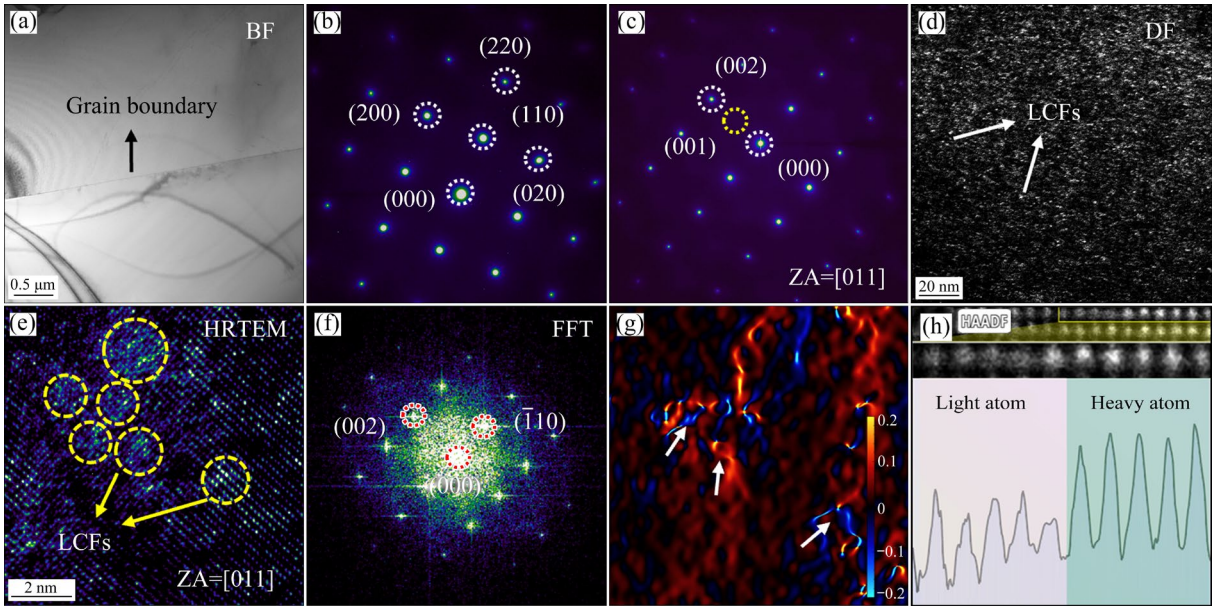

Fig. 3 High magnification TEM microstructure of LDED-RMPEA: (a) Bright-field (BF) image of sample; (b) Diffraction pattern corresponding to matrix; (c) Original diffraction pattern along [011] zone axis (ZA); (d) Dark-field image of matrix taken in diffraction condition of yellow dashed circle in (c); (e) High-resolution (HR) TEM image of matrix with nanocluster; (f) Fast Fourier transform (FFT) pattern corresponding to (e); (g) Lattice dilatation field of (e); (h) HAADF image of LCF under [001] zone axis and column-by-column line scan profile

composition families. These atomic-scale LCFs act as metastable precursors to such extreme phases, exacerbated by rapid non-equilibrium solidification during laser additive manufacturing [30].

3.2 Mechanical behavior and microstructural evolution of alloy

The room-temperature mechanical behavior of the alloy and its microstructural characteristics after deformation are presented in Fig. 4. This alloy exhibits exceptional plasticity at room temperature, showing no fracture or surface cracking even when compressed by 80%. The sample is compressed from a cylindrical shape to a pancake shape, with a yield strength of 1095 MPa and a maximum compressive stress of 4154 MPa during deformation, as shown in Fig. 4(a). Despite increased engineering stress, the alloy exhibits deformation softening at later stages, as shown by the red true stress−strain curve in Fig. 4(b). The strain hardening rate (SHR) curve shows that the alloy undergoes three deformation stages: hardening, stabilization, and softening, as indicated by the green curve in Fig. 4(b). The EBSD results of the deformed sample reveal that the grain morphology has significantly changed due to deformation, as shown in Figs. 4(c, d). The deformation characteristics of the grains can be categorized into two types. The first type includes uniformly deformed grains, such as G1 grain, which transform from columnar to elongated grains oriented perpendicularly to the force axis. The second type involves the formation of additional kink bands within the grains, as observed in G2 and G3 grains. The coordinated deformation of these two-grain types leads to the exceptional plasticity of alloy.

We thoroughly analyzed the first type of uniformly deformed G1 grain and found a high Schmid factor (SF) value close to 0.5, as revealed in the SF mapping. This indicates that the grain is favorably oriented in a soft deformation orientation, as shown in Figs. 4(e, g). At least three distinct types of slip traces are visible in the IQ diagram of Fig. 4(f). The initiation of multi-system slip alleviates stress concentration within the grain, preventing microcrack formation even under extensive deformation. The analysis of the G1 grain's orientation deviation

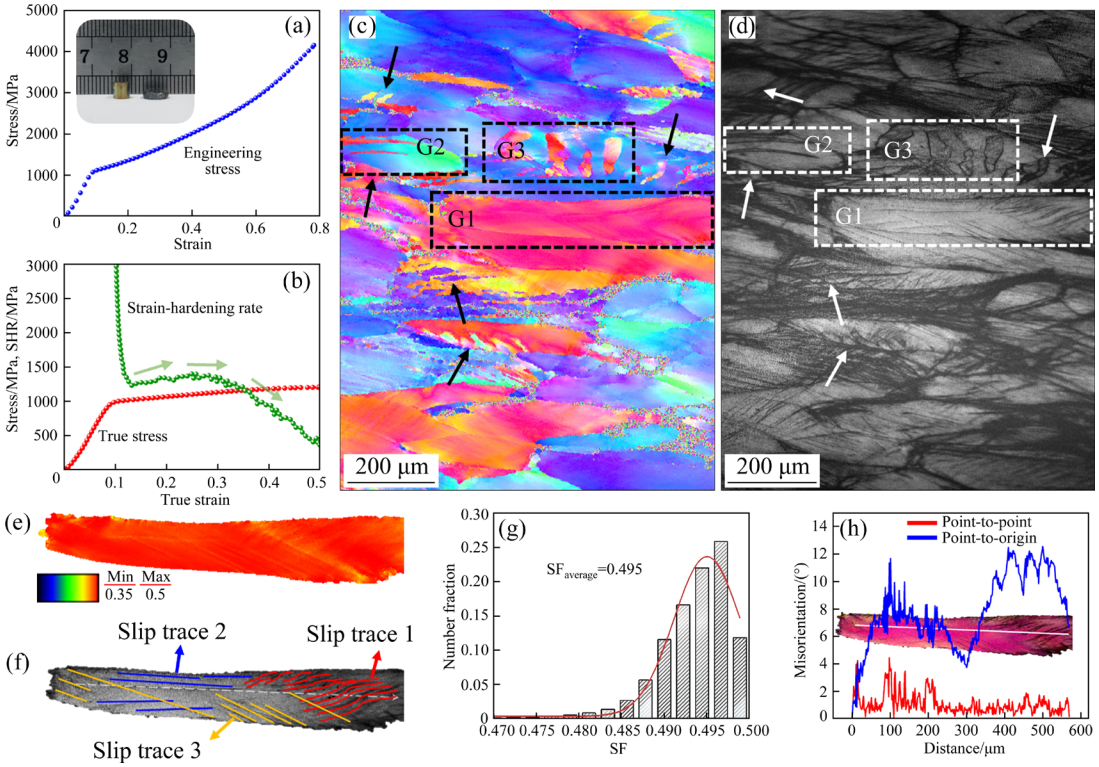

Fig. 4 Compression deformation behavior and corresponding EBSD results after deformation: (a) Compressive engineering stress−strain curve of LDED-RMPEA (Inset: Macroscopic photographs of sample before and after deformation); (b) True stress−strain curve and strain−strain hardening rate curve of sample; (c) IPF maps of sample after deformation; (d) IQ map of sample after deformation; (e, f) SF map and IQ map of G1 grain, respectively; (g) SF statistical chart of G1 grain; (h) Misorientation variation along white line of G1 grain

along the elongation direction shows that the grain maintains a favorable rotation during deformation, with an internal orientation difference not exceeding 12°. The primary characteristics of the first type of uniformly deformed grains are as described above.

The primary deformation feature of the second type of grains is the unusual kink bands, which show significant orientation deviation from the matrix. These deviations are evident through color difference in the IPF image, particularly in the selected G2 and G3 grains (Fig. 4(c) and Figs. 5(a, d)). A detailed description of the kink band characteristics is provided, as research on kink behavior in MPEAs remains limited. Under identical external loading conditions, the direction of kink bands varies among different grains, as exemplified by G2 and G3 grains. This suggests that the direction of the force axis is not the sole factor influencing kink behavior. The rotation of specific grain regions induces kink bands, and thus the rotation axis direction of the grain kink behavior in G2 grain can be identified as [110] from the pole diagram in Fig. 5(c). Furthermore, kink bands typically form in grains with lower SF values, which are tough-oriented and difficult to deform; however, the kink bands themselves are soft deformation regions with higher SF values. This mechanism is crucial for tough-oriented grains, as it significantly alleviates stress concentration. Another notable observation is the lower SF value at the edge of the kink band, as indicated by the white arrows in Figs. 5(b, e). Given the strong correlation between kink behavior and SF value, the lower SF value is considered the starting point of the kink band, while the higher SF value at

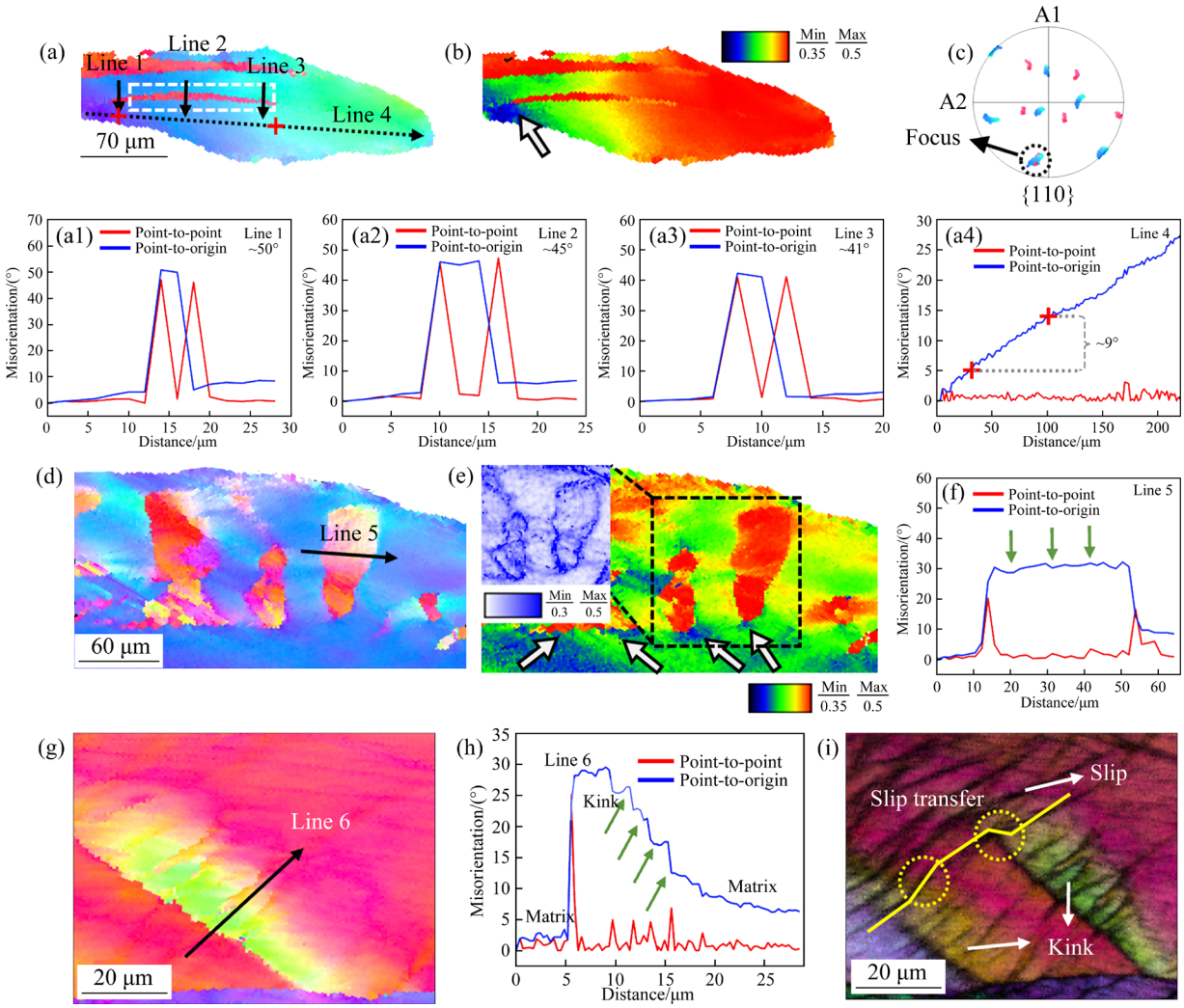

Fig. 5 EBSD results of particular G2 and G3 grains: (a) IPF map of G2 grain; (b) SF map of G2 grain; (c) {110} pole figure of kink band with matrix in (a); (a1−a4) Misorientation along Lines 1−4 in (a); (d) IPF map of G3 grain; (e) SF map of G3 grain (Inset: Kernel average misorientation (KAM) map; (f) Misorientation along Line 5 in (d); (g) IPF map of not yet fully matured kink band; (h) Misorientation along Line 6 in (g); (i) IPF + IQ mapping corresponding to (g)

the other end serves as the endpoint. The kink bands exhibited variability in both width and length, with the orientation characteristics at the starting and ending points showing slight differences. The orientation deviation between different regions of the kink bands and the matrix varies along the elongation direction, as shown in Figs. 5(a1−a3), with orientation differences ranging from 41° to 50°. The overall orientation deviation angle within the grains significantly exceeds that of the G1 grain by 12°, showing a continuous gradient increase from 0° to 27°. The difference between the starting and ending points of the kink band corresponds to the incremental rotation of the matrix grains (approximately 9°, as shown in Figs. 5(a, a4) (red cross)), indicating an adaptive coordination process of grain rotation within the kink band. Orientation fluctuations are observed along the width of wider kink bands (approximately 40 μm), as indicated by the green arrows, which shows that the soft-oriented kink region has also experienced deformation. This adaptive mechanism enables the alloys to undergo further plastic deformation, even when subjected to exceptionally high strains in unfavorable orientations, a process that traditional twinning mechanisms cannot accommodate. The orientation difference between various kinks and the matrix varies. For instance, in G2 and G3 grains, the orientation difference between kinks and matrix is 41°−50° and 30°, respectively. In contrast, deformation twins exhibit a strictly defined crystal orientation relationship with the matrix. For example, {332}⟨113⟩ and {112}⟨111⟩ twins typically exhibit misorientations of 50.5° and 70.5°, respectively. Furthermore, misorientation within twin bands remains constant, unlike the variable misorientation observed in kink bands.

A high density of geometrically necessary dislocations (GNDs) is observed at the kink band boundary, as revealed by the KAM diagram in Fig. 5(e). This suggests a close correlation between kink band formation and GNDs, indicating that kink boundaries may act as obstacles to dislocation movement. Unlike twinning, kink bands are characterized by upper and lower interfaces composed of two rows of edge dislocations with opposing signs. Notably, not all kink band boundaries observed in the experiment are abrupt relative to the matrix. While the kink bands in the G2 and G3 grains exhibit sharp boundaries, the grain rotation is not an instantaneous process. As shown in Figs. 5(g, h), a kink band in an intermediate stage of formation was observed. The gradient distribution of orientation steps on the diffusing side of the band vividly illustrates the progression of kink propagation. Furthermore, slip transfer induced by the kinking process is evident from the IPF + IQ overlay map in Fig. 5(i), which reveals that the slip deformation is more tortuous. This further contributes to energy dissipation while relieving stress concentration.

Double kink behavior was observed in the alloy, with the secondary kink occurring within the primary kink, as shown in Fig. 6(a). The misorientation between the primary kink and the matrix is 40°, while that between the secondary kink and the primary kink is approximately 10°, as shown in Fig. 6(b). Furthermore, it is found that both kink behaviors are associated with the same [211] rotation axis, as shown in Fig. 6(c). The occurrence of double kink behavior provides strong evidence for the distinct nature of kink behavior in plastic deformation. When the primary kink is insufficient to fully alleviate stress concentration, a secondary kink is activated.

The kink boundary, as a pure tilt boundary formed by the localization of edge dislocations, allows dislocation characteristics to be identified based on the rotation axis. This process can be explained using a simplified beam model [31]. Two extreme cases correspond to tough and soft orientations under resolved shear stress, as shown in Figs. 7(a, b), assuming negligible elastic strain. When both the slip plane and slip direction are parallel to the displacement direction, dislocation slip leads to displacement without storing any dislocations after deformation. This corresponds to soft orientation grains that are easily deformed, as shown in Fig. 7(a). In contrast, when the slip plane is perpendicular to the displacement direction, slip is suppressed, corresponding to tough orientation grains. Shear strain is introduced into the beam model component in this case, and further lattice rotation is required to prevent neighboring units from overlapping. However, when these units rejoin, some positive and negative dislocations cancel out on the surface, while the remaining dislocations are retained at the unit interface as GNDs. The accumulation of dislocations in the curvature region results in lattice bending around the rotation axis,

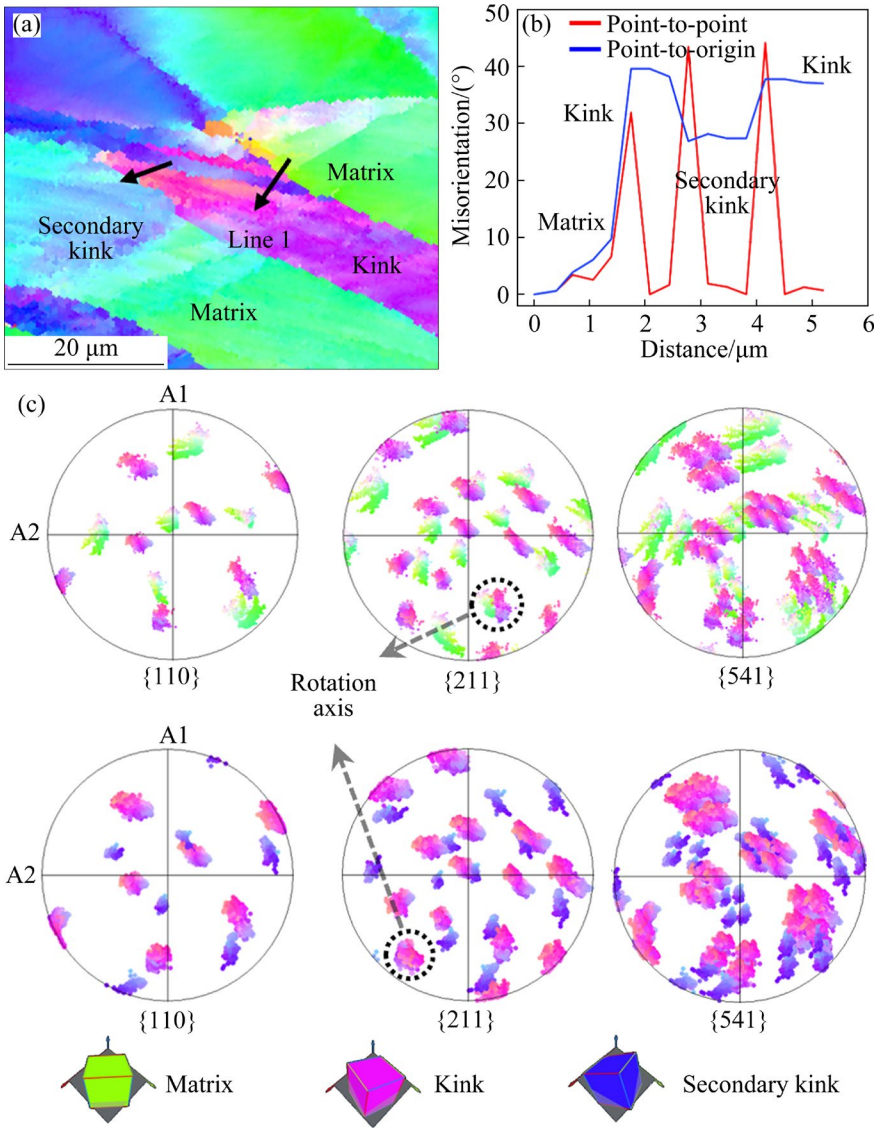

Fig. 6 EBSD results of double kink behavior: (a) IPF map of matrix, primary kink, and secondary kink; (b) Misorientation along Line 1 in (a); (c) {110}, {211}, and {541} pole figures of double kink bands in (a)

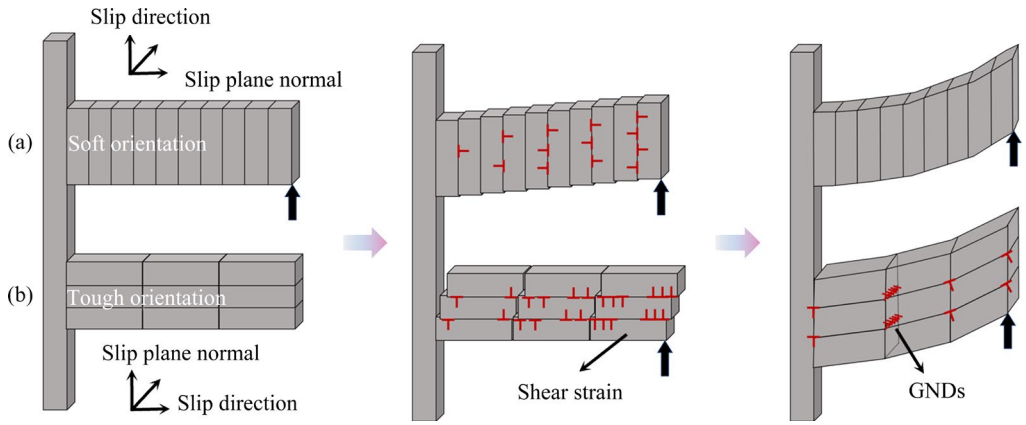

Fig. 7 Schematic diagrams of beam model: (a) Soft orientation; (b) Tough orientation

transforming this bending region into the kink band. In summary, the displacement of tough orientation grains is facilitated by a combination of plastic slip and lattice rotation, as shown in Fig. 7(b). This explains why the kink boundary exhibits a high local strain distribution. Based on the analysis of slip-

induced lattice rotation, the relationship of the slip plane normal (n), the magnitude of Burgers vector (b), and the rotation axis (T) is given by $T=\gamma bn$, where γ represents the shear strain. The physical interpretation of this equation is that the rotation axis lies within the slip plane and is perpendicular to the Burgers vector [32]. The dominant slip mode in the deformed grain can be determined based on the known rotation axis. This indicates that the [110] rotation axis in Fig. 5(c) corresponds to the (a/2⟨111⟩{211}) dislocation slip mode, while the double kink in Fig. 6(c) corresponds to the (a/2⟨111⟩{110}) dislocation slip mode.

The dislocation behavior characteristics of LDED-RMPEAs were further analyzed. A clear interaction between LCFs and dislocations is observed in Fig. 8(a). LCFs continuously pin dislocations, leading to wavy dislocation lines. The distribution density of LCFs in the matrix is significantly higher than that in traditional precipitation, causing local nanoscale obstruction to dislocations. As shown in Fig. 8(b), MPEAs lack a clear distinction between solute and solvent, making dislocation movement more complex than in SPEAs with solid solution strengthening [33]. During the deformation process, mixed dislocations are predominant, while edge dislocations are relatively scarce, as shown in Fig. 8(c). The dislocation types are further detailed in Fig. S2 in SM. In BCC metals and alloys, edge dislocations are rarely observed due to their high mobility. In contrast, the presence of edge dislocations in this alloy indicates decreased dislocation mobility within RMPEAs. The reduction in dislocation mobility may be attributed to the widespread LCFs and lattice distortion within the matrix, as highlighted by yellow circles in Figs. 8(a, c). These defects introduce additional hindrance and pinning effects at the nanoscale. As a result, dislocations move slowly and discontinuously rather than smoothly and rapidly [34]. Slip microbands observed on the fractured specimen, as shown in Fig. S3 in SM, further indicate that planar slip is the primary deformation mechanism. Figure 8(d) illustrates the accumulation of GNDs at the kink band's boundary and the appearance of additional dislocations within the band. Significant deformation leads to the formation of dislocation cell structures within the kink band, as shown in

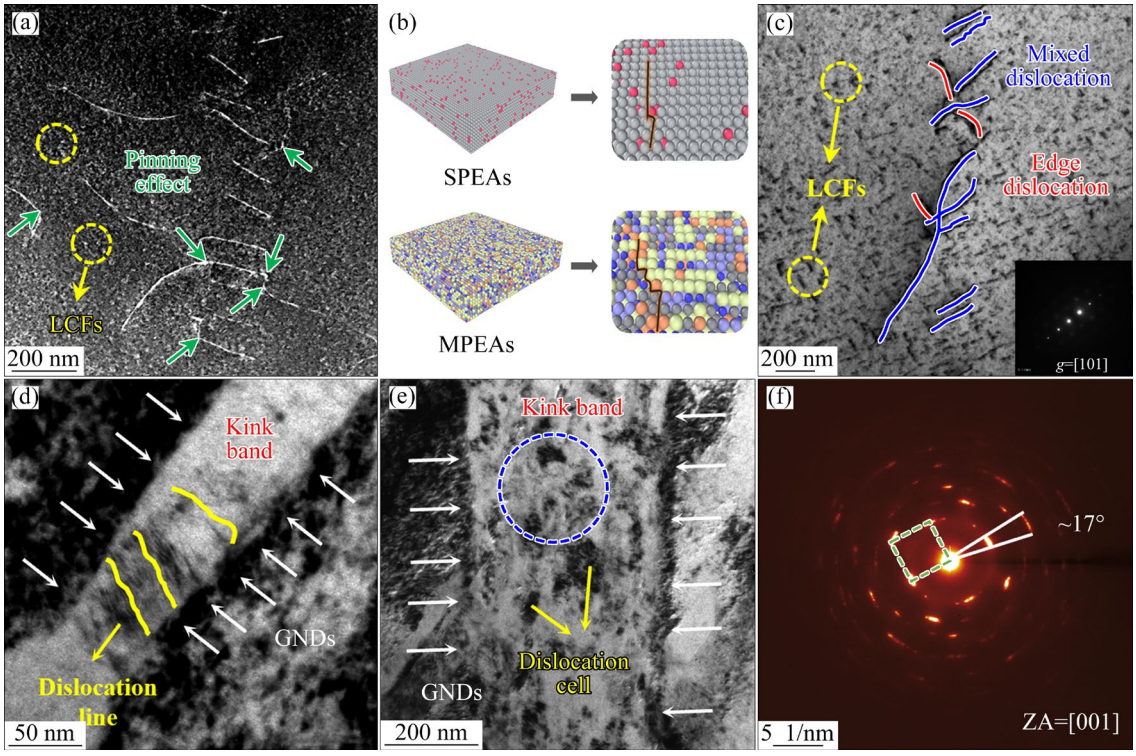

Fig. 8 High magnification TEM microstructure of LDED-RMPEA after deformation: (a) Dark-field image of typical dislocation characteristic; (b) Diagram illustrating solute environment characteristics of SPEAs and MPEAs; (c) Dislocation type of alloy after deformation; (d) Bright-field image of kink band and dislocation lines; (e) Bright-field image of kink band after deformation containing many dislocation cells; (f) Diffraction pattern of dislocation cells within kink bands corresponding to blue circle in (e)

Figs. 8(e, f). These dislocation cells exhibit substantial deformation, resulting in lattice orientation variation of approximately 17°.

The following section provides a detailed analysis and summary of the conditions that promote kink formation. Firstly, the limited number of slip systems and the depletion of movable slip systems result in the formation of abnormally high strain concentration areas, particularly in grains with tough orientations (low SF). This strain concentration serves as a primary prerequisite for kink excitation. In contrast, soft-orientation grains with high SF values coordinate deformation through the activation of multiple slip systems, thereby alleviating stress concentration. Secondly, the activation of the appropriate slip system is crucial for the formation of kinked GNDs. In the case of the G2 grain, the $\{112\}\langle 111\rangle$ slip mode is activated, with the loading axis direction in the crystal coordinate system being $[\bar{3}\,\bar{3}\,\bar{4}]$. The calculated SF values for all 48 slip systems in this grain are listed in Table S1 in SM, which were analyzed to determine the slip system activation responsible for G2 grain kinking. The largest value of cos φ was found for the (112)[111] slip system, approaching 0.98, indicating that the slip system required for kink formation is related to the angle between the loading axis and the normal of the slip plane. It is speculated that when hard-oriented grains experience depletion of slip systems, the slip system closest to the loading axis is passively activated as the external force increases, despite not being the most favorable slip system. This leads to the accumulation of GNDs necessary for lattice rotation. Finally, the influence of LCFs in the matrix on dislocation behavior must be considered, particularly their impact on dislocation mobility. Although plastic deformation in the alloy is primarily controlled by the slip of mixed dislocations, the presence of LCFs in RMPEAs modifies dislocation behavior, promoting the activation of edge dislocations within the slip systems. This, in turn, establishes conditions favorable for forming GNDs necessary for kink band development. In high-strain regions, such as stress concentration zones near grain boundaries, edge dislocations enhance kinking behavior on the {110} and {112} planes. This process continuously rotates the lattice, thereby accommodating local strain, preventing the nucleation of micro-voids within grains, and effectively dispersing damage.

4 Conclusions

(1) The kink behavior exhibits three key characteristics. Firstly, the misorientation between the kink and the matrix is not stationary, and the misorientation within the kink band also varies. Secondly, the kink band represents a soft orientation with higher SF values compared with the matrix, and the kink band boundary is characterized by a high density of GNDs. Finally, kink formation is a gradual rotational diffusion process rather than an instantaneous event, differing from twinning behavior.

(2) The absence of numerous activatable slip systems in tough-orientation grains (low SF value) represents the primary condition for kink excitation. Under external loading, the slip system closest to the loading axis is passively activated, thereby accumulating the GNDs necessary for lattice rotation. Additionally, the widespread presence of LCFs within the matrix reduces the slip rate of dislocations, thereby facilitating their accumulation.

(3) Throughout the deformation process, kink behavior facilitates continuous lattice rotation, which accommodates nearby high strains, prevents micro-void nucleation within grains, and effectively disperses damage. The kink bands self-adjust with grain rotation, enabling further plastic deformation even under unfavorable loading directions. This is something that traditional twinning mechanisms cannot accommodate. Moreover, double kink formation may occur when stress concentration in the primary kink is insufficiently relieved, thereby enhancing the deformability of the RMPEA.

CRediT authorship contribution statement

Yan-song ZHANG: Conceptualization, Methodology, Investigation, Formal analysis, Writing − Original draft, Visualization; **Hua-ming WANG:** Writing − Review & editing, Project administration; **Yan-yan ZHU:** Writing − Review & editing, Project administration, Supervision; **Bing-sen LIU:** Writing − Review & editing; **Zhuo LI:** Project administration, Supervision; **Bing SU:** Writing − Review & editing, Validation; **Chun-jie SHEN:** Writing − Review & editing.

Declaration of competing interest

The authors declare that they have no known

competing financial interests or personal relationships that could have appeared to influence the work reported in this paper.

Supplementary Material

Supplementary Material in this paper can be found at: https://tnmsc.csu.edu.cn/download/11-p0830-2024-0841-Supplementary_Materials.pdf.

References

[1] LI Tian-xin, MIAO Jun-wei, GUO En-yu, HUANG He, WANG Jun, LU Yi-ping, WANG Tong-min, CAO Zhi-qiang, LI Ting-ju. Tungsten-containing high-entropy alloys: A focused review of manufacturing routes, phase selection, mechanical properties, and irradiation resistance properties [J]. Tungsten, 2021, 3(2): 181−196.

[2] GUO Lin, GU Ji, DAI Yi-long, LIN Jian-guo, SONG Min. Heterogeneous microstructure and mechanical properties of carbon-doped FeCoCrNiMn high-entropy alloy [J]. Transactions of Nonferrous Metals Society of China, 2024, 34(6): 1893−1907.

[3] GAO Xue-feng, CHEN Yao, REN Hao, QIN Gang, ZHOU Qi-wen, CHEN Rui-run, GUO Jing-jie. Tensile properties and strengthening behavior of CoCrFeNiW high entropy alloys with heterogeneous structures [J]. Transactions of Nonferrous Metals Society of China, 2024, 34(3): 890−904.

[4] ZHANG Yong, ZHOU Yun-jun, LIN Jun-pin, CHEN Guo-liang, LIAW P K. Solid-solution phase formation rules for multi-component alloys [J]. Advanced Engineering Materials, 2008, 10(6): 534−538.

[5] LI Tian-xin, LU Yi-ping, LI Zhi-qiang, WANG Tong-min, LI Ting-ju. Hot deformation behavior and microstructure evolution of non-equimolar $Ti_2ZrHfV_{0.5}Ta_{0.2}$ refractory high-entropy alloy [J]. Intermetallics, 2022, 146: 107586.

[6] LI Tian-xin, JIAO Wen-na, MIAO Jun-wei, LU Yi-ping, GUO En-yu, WANG Tong-min, LI Ting-ju, LIAW P K. A novel ZrNbMoTaW refractory high-entropy alloy with in-situ forming heterogeneous structure [J]. Materials Science and Engineering: A, 2021, 827: 142061.

[7] SENKOV O N, WILKS G B, SCOTT J M, MIRACLE D B. Mechanical properties of $Nb_{25}Mo_{25}Ta_{25}W_{25}$ and $V_{20}Nb_{20}Mo_{20}Ta_{20}W_{20}$ refractory high entropy alloys [J]. Intermetallics, 2011, 19(5): 698−706.

[8] WANG Zheng-qi, WU Hong-hui, WU Yuan, HUANG Hai-long, ZHU Xiang-yu, ZHANG Ying-jie, ZHU Hui-hui, YUAN Xiao-yuan, CHEN Qiang, WANG Shu-dao, LIU Xiong-jun, WANG Hui, JIANG Sui-he, KIM M J, LU Zhao-ping. Solving oxygen embrittlement of refractory high-entropy alloy via grain boundary engineering [J]. Materials Today, 2022, 54: 83−89.

[9] HUANG Hai-long, WU Yuan, HE Jun-yang, WANG Hui, LIU Xiong-jun, AN Ke, WU Wei, LU Zhao-ping. Phase-transformation ductilization of brittle high-entropy alloys via metastability engineering [J]. Advanced Materials, 2017, 29(30): 1701678.

[10] SONI V, SENKOV O N, GWALANI B, MIRACLE D B, BANERJEE R. Microstructural design for improving ductility of an initially brittle refractory high entropy alloy [J]. Scientific Reports, 2018, 8(1): 8816.

[11] SENKOV O N, CROSSMAN B, RAO S I, COUZINIE J P, MIRACLE D B, BUTLER T M, BANERJEE R, MILLS M. Mechanical properties of an $Al_{10}Nb_{20}Ta_{15}Ti_{30}V_5Zr_{20}$ A2/B2 refractory superalloy and its constituent phases [J]. Acta Materialia, 2023, 254: 119017.

[12] ZHANG Cheng, WANG Hao-ren, WANG Xin-yi, TANG Y T, YU Qin, ZHU Chao-yi, XU Ming-jie, ZHAO Shi-teng, KOU Rui, WANG Xin, MACDONALD B E, REED R C, VECCHIO K S, CAO Peng-hui, RUPERT T J, LAVERNIA E J. Strong and ductile refractory high-entropy alloys with super formability [J]. Acta Materialia, 2023, 245: 118602.

[13] HESS J B, BARRETT C S. Structure and nature of kink bands in zinc [J]. JOM, 1949, 1(9): 599−606.

[14] ZHANG Yong-yun, QIN Bai-liang, OUYANG Di, LIU Lin, FENG Chuang-shi, YAN Yu-qiang, YE Shu-long, KE Hai-bo, CHAN K C, WANG Wei-hua. Strong yet ductile refractory high entropy alloy fabricated via additive manufacturing [J]. Additive Manufacturing, 2024, 81: 104009.

[15] CUI Ding-cong, GUO Bo-jing, YANG Zhong-sheng, LIU Xin, WANG Zhi-jun, LI Jun-jie, WANG Jin-cheng, HE Feng. Unraveling microstructure and mechanical response of an additively manufactured refractory TiVHfNbMo high-entropy alloy [J]. Additive Manufacturing, 2024, 84: 104126.

[16] GOU Shu-yuan, GAO Ming-yu, SHI Yun-zhu, LI Shun-chao, FANG You-tong, CHEN Xin-huan, CHEN Huai-can, YIN Wen, LIU Jia-bin, LEI Zhi-feng, WANG Hong-tao. Additive manufacturing of ductile refractory high-entropy alloys via phase engineering [J]. Acta Materialia, 2023, 248: 118781.

[17] HE Ji, FU Hua-meng, LIU Cui-rong, ZHU Zheng-wang, ZHANG Long, LI Zheng-kun, LI Hong, ZHANG Hai-feng. Effects of aging on microstructure and wear resistance of laser cladding $Mo_{0.5}NbTiVCr_{0.25}$ high-entropy alloy coating [J]. Transactions of Nonferrous Metals Society of China, 2024, 34(7): 2219−2230.

[18] CAO Tang-qing, GUO Wen-qi, LU Wang, XUE Yun-fei, LU Wen-jun, SU Jing, LIEBSCHER C H, LI Chang, DEHM G. Strain rate dependent deformation behavior of BCC-structured $Ti_{29}Zr_{24}Nb_{23}Hf_{24}$ high entropy alloy at elevated temperatures [J]. Journal of Alloys and Compounds, 2022, 891: 161859.

[19] WU Ming-xu, WANG Shu-bin, XIAO Fei, ZHU Guo-liang, YANG Chao, SHU Da, SUN Bao-de. Dislocation glide and mechanical twinning in a ductile VNbTi medium entropy alloy [J]. Journal of Materials Science & Technology, 2022, 110: 210−215.

[20] WANG Shu-bin, WU Ming-xu, SHU Da, ZHU Guo-liang, WANG Dong-hong, SUN Bao-de. Mechanical instability and tensile properties of TiZrHfNbTa high entropy alloy at cryogenic temperatures [J]. Acta Materialia, 2020, 201: 517−527.

[21] STEPANOV N D, YURCHENKO N Y, SOKOLOVSKY V S, TIKHONOVSKY M A, SALISHCHEV G A. An $AlNbTiVZr_{0.5}$ high-entropy alloy combining high specific strength and good ductility [J]. Materials Letters, 2015, 161: 136−139.

[22] ZENG Shuai, ZHU Yu-hui, LI Wei, ZHANG Hong-wei,

ZHANG Hai-feng, ZHU Zheng-wang. A single-phase $Ti_3Zr_{1.5}NbVAl_{0.25}$ refractory high entropy alloy with excellent combination of strength and toughness [J]. Materials Letters, 2022, 323: 132548.

[23] ZENG Shuai, ZHOU Yong-kang, LI Huan, ZHANG Hong-wei, ZHANG Hai-feng, ZHU Zheng-wang. Microstructure and mechanical properties of lightweight $Ti_3Zr_{1.5}NbVAl$ (x=0, 0.25, 0.5 and 0.75) refractory complex concentrated alloys [J]. Journal of Materials Science & Technology, 2022, 130: 64−74.

[24] ZHANG Yan-song, WANG Hua-ming, ZHU Yan-yan, ZHANG Shu-quan, CHENG Fang, YANG Jun-wei, SU Bing, YANG Chen. High specific yield strength and superior ductility of a lightweight refractory high-entropy alloy prepared by laser additive manufacturing [J]. Additive Manufacturing, 2023, 77: 103813.

[25] WANG Tao, ZHU Yan-yan, ZHANG Shu-quan, TANG Hai-bo, WANG Hua-ming. Grain morphology evolution behavior of titanium alloy components during laser melting deposition additive manufacturing [J]. Journal of Alloys and Compounds, 2015, 632: 505−513.

[26] FANG X T, HE G Z, ZHENG C, MA L X, KAOUMI D, LI Y S, ZHU Y T . Effect of heterostructure and hetero-deformation induced hardening on the strength and ductility of brass [J]. Acta Materialia, 2020, 186: 644−655.

[27] BU Ye-qiang, WU Yuan, LEI Zhi-feng, YUAN Xiao-yuan, WU Hong-hui, FENG Xiao-bin, LIU Jia-bin, DING Jun, LU Yang, WANG Hong-tao, LU Zhao-ping, YANG Wei. Local chemical fluctuation mediated ductility in body-centered-cubic high-entropy alloys [J]. Materials Today, 2021, 46: 28−34.

[28] WU Yuan, ZHANG Fei, YUAN Xiao-yuan, HUANG Hai-long, WEN Xiao-can, WANG Yi-han, ZHANG Meng-yuan, WU Hong-hui, LIU Xiong-jun, WANG Hui, JIANG Sui-he, LU Zhao-ping. Short-range ordering and its effects on mechanical properties of high-entropy alloys [J]. Journal of Materials Science & Technology, 2021, 62: 214−220.

[29] XU Bo-wen, DUAN Hui-chao, CHEN Xue-fei, WANG Jing, MA Yan, JIANG Ping, YUAN Fu-ping, WANG Yan-dong, REN Yang, DU Kui, WEI Yue-guang, WU Xiao-lei. Harnessing instability for work hardening in multi-principal element alloys [J]. Nature Materials, 2024, 23(6): 755−761.

[30] REN Jie, ZHANG Yin, ZHAO De-xin, CHEN Yan, GUAN Shuai, LIU Yan-fang, LIU Liang, PENG Si-yuan, KONG Fan-yue, POPLAWSKY J D, GAO Guan-hui, VOISIN T, AN Ke, WANG Y MORRIS, XIE KEIVIN Y, ZHU Ting, CHEN Wen. Strong yet ductile nanolamellar high-entropy alloys by additive manufacturing [J]. Nature, 2022, 608(7921): 62−68.

[31] YAMASAKI M, HAGIHARA K, INOUE S I, HADORN J P, KAWAMURA Y. Crystallographic classification of kink bands in an extruded Mg−Zn−Y alloy using intragranular misorientation axis analysis [J]. Acta Materialia, 2013, 61(6): 2065−2076.

[32] WANG Shu-bin, WU Ming-xu, SHU Da, SUN Bao-de. Kinking in a refractory $TiZrHfNb_{0.7}$ medium-entropy alloy [J]. Materials Letters, 2020, 264: 127369.

[33] WANG Shao-ping, XU Jian. (TiZrNbTa)−Mo high-entropy alloys: Dependence of microstructure and mechanical properties on Mo concentration and modeling of solid solution strengthening [J]. Intermetallics, 2018, 95: 59−72.

[34] WANG Fu-lin, BALBUS G H, XU Shuo-zhi, SU Yan-qing, SHIN J, ROTTMANN P F, KNIPLING K E, STINVILLE J C, MILLS L H, SENKOV O N, BEYERLEIN I J, POLLOCK T M, GIANOLA D S. Multiplicity of dislocation pathways in a refractory multiprincipal element alloy [J]. Science, 2020, 370(6512): 95−101.

激光增材制造难熔多主元合金的变形扭折行为

张言嵩[1,2]，王华明[1,2]，朱言言[1,2]，刘炳森[1,2]，李 卓[1,2]，苏 冰[1,2]，申春杰[1,2]

1. 北京航空航天大学 材料科学与工程学院，北京 100191；
2. 大型金属构件增材制造国家工程实验室，北京 100191

摘 要：采用室温压缩试验、电子背散射衍射(EBSD)、透射电镜(TEM)和高角环形暗场成像(HAADF)技术研究激光定向能量沉积(LDED)技术制备的富含局部化学波动(LCFs)的难熔多主元合金(RMPEAs)在变形过程中的扭折特征及其激活机制。结果表明：扭折是个渐进的旋转扩散过程，在此过程中，扭折与基体之间的取向差不固定。低的 Schmid 因子值是扭折激发的先决条件，最靠近加载轴的滑移系统在外力作用下被动激活，积累了旋转晶格所需的几何位错密度(GNDs)。基体中广泛存在的 LCFs 降低了刃型位错的迁移速率，促进了 GNDs 的累积，从而促进扭折行为的发生。变形过程中，扭折行为的发生使晶格不断旋转，适应附近的异常高应变，当主扭结中的应力集中无法完全释放时，二次扭折会被激活。

关键词：难熔多主元合金；塑性变形；扭折带；Schmid 因子；局部化学波动

(Edited by Xiang-qun LI)